

LETTER TO THE EDITOR

# Detection of vibrationally excited C<sub>6</sub>H in the cold prestellar core TMC-1 with the QUIJOTE line survey<sup>★</sup>

J. Cernicharo<sup>1</sup>, R. Fuentetaja<sup>1</sup>, M. Agúndez<sup>1</sup>, C. Cabezas<sup>1</sup>, B. Tercero<sup>2,3</sup>, N. Marcelino<sup>2,3</sup>, and P. de Vicente<sup>3</sup>

<sup>1</sup> Dept. de Astrofísica Molecular, Instituto de Física Fundamental (IFF-CSIC), C/ Serrano 121, 28006 Madrid, Spain.  
e-mail: jose.cernicharo@csic.es, r.fuentetaja@csic.es

<sup>2</sup> Observatorio Astronómico Nacional (OAN, IGN), C/ Alfonso XII, 3, 28014, Madrid, Spain.

<sup>3</sup> Centro de Desarrollos Tecnológicos, Observatorio de Yebes (IGN), 19141 Yebes, Guadalajara, Spain.

Received 05/11/2023; accepted 17/11/2023

## ABSTRACT

In this work, we present the detection of twelve doublets with quantum numbers of  $N=12-11$  to  $N=17-16$  of the  $\nu_{11}(\mu^2\Sigma)$  vibrationally excited state of C<sub>6</sub>H towards TMC-1. This marks the first time that an excited vibrational state of a molecule has been detected in a cold starless core. The data are part of the QUIJOTE line survey gathered with the Yebes 40m radio telescope. The line intensities have been aptly reproduced with a rotational temperature of  $6.2\pm 0.4$  K and a column density of  $(1.2\pm 0.2)\times 10^{11}$  cm<sup>-2</sup>. We also analysed the ground state transitions of C<sub>6</sub>H, detecting fourteen lines with quantum numbers of  $J = 23/2-21/2$  to  $J = 35/2$  for each of the two <sup>2</sup>Π<sub>3/2</sub> and <sup>2</sup>Π<sub>1/2</sub> ladders. It is not possible to model the intensities of all the transitions of the ground state simultaneously using a single column density. We considered the two ladders as two different species and found that the rotational temperature is the same for both ladders,  $T_{rot}(\text{<sup>2</sup>Π}_{3/2})=T_{rot}(\text{<sup>2</sup>Π}_{1/2})=6.2\pm 0.2$ , achieving a result that is comparable to that of the  $\nu_{11}(\mu^2\Sigma)$  state. The derived column densities are  $N(\text{<sup>2</sup>Π}_{3/2})=(6.2\pm 0.3)\times 10^{12}$  cm<sup>-2</sup> and  $N(\text{<sup>2</sup>Π}_{1/2})=(8.0\pm 0.4)\times 10^{10}$  cm<sup>-2</sup>. The fraction of C<sub>6</sub>H molecules in its <sup>2</sup>Π<sub>3/2</sub>, <sup>2</sup>Π<sub>1/2</sub>, and  $\nu_{11}(\mu^2\Sigma)$  states is 96.8 %, 1.3 %, and 1.9 %, respectively. Finally, we report that this vibrational mode has also been detected towards the cold cores Lupus-1A and L1495B, as well as the low-mass star forming cores L1527 and L483, with fractions of C<sub>6</sub>H molecules in this mode of 3.8 %, 4.1 %, 14.8 %, and 6 %, respectively.

**Key words.** molecular data — line: identification — ISM: molecules — ISM: individual (TMC-1) — astrochemistry

## 1. Introduction

The first detection of C<sub>6</sub>H in space has been achieved towards TMC-1 (Suzuki et al. 1986; Cernicharo et al. 1987) and in the direction of the carbon rich star IRC+10216 (Guélin et al. 1987). The identification was based on ab initio calculations of the structure and electronic state of the molecule, which indicate that the ground state could be a <sup>2</sup>Π state (Murakami et al. 1988), contrary to CCH and C<sub>4</sub>H, which have a <sup>2</sup>Σ<sup>+</sup> ground state. The detection in space of two series of harmonically lines with half-integer quantum numbers (lines from the <sup>2</sup>Π<sub>3/2</sub> and the <sup>2</sup>Π<sub>1/2</sub> ladders, Suzuki et al. 1986; Guélin et al. 1987; Cernicharo et al. 1987) clearly supported the identification. Nevertheless, the assignment of the observed lines to this species was confirmed by the generation of the radical and the observation of its rotational spectrum in the laboratory (Pearson et al. 1988). The spin orbit constant,  $A_{SO}$ , is  $-15.04$  cm<sup>-1</sup> (Linnartz et al. 1999). Hence, the energy of the <sup>2</sup>Π<sub>1/2</sub> ladder is  $\sim 22$  K above the <sup>2</sup>Π<sub>3/2</sub> one.

C<sub>6</sub>H has six stretching modes,  $\nu_1 - \nu_6$ , and five bending modes,  $\nu_7 - \nu_{11}$  (Brown et al. 1999). The  $\nu_{11}$  mode is the bending with the lowest energy, which has been estimated to be between  $120$  and  $134$  cm<sup>-1</sup> (Brown et al. 1999; Cao & Peyerimhoff 2001). This bending mode produces a <sup>2</sup>Δ and two <sup>2</sup>Σ vibronic modes. One of the <sup>2</sup>Σ states, labelled as  $\mu^2\Sigma$  by Zhao

et al. (2011), and the <sup>2</sup>Δ one have been identified in IRC+10216 during a search for C<sub>5</sub>N<sup>-</sup> (Cernicharo et al. 2008). The assignment was subsequently confirmed by extensive laboratory spectroscopy of C<sub>6</sub>H in its  $\nu_{11}$  vibrationally excited state (Gottlieb et al. 2010).

The  $\nu_{11}$  vibrational mode is affected by a strong Renner-Teller interaction resulting from the coupling of the degenerate bending vibration with the orbital angular momentum of an unpaired electron (Zhao et al. 2011). This coupling produces a considerably lowering of the energy of the  $\mu^2\Sigma$  vibronic mode. This energy has been estimated to be  $20\pm 10$  K (Gottlieb et al. 2010). In a detailed study involving the electronic transition B<sup>2</sup>Π-X<sup>2</sup>Π, this energy has been determined to be  $11.0\pm 0.8$  cm<sup>-1</sup> (Zhao et al. 2011), namely, around 15.8 K. This value is below the energy the <sup>2</sup>Π<sub>1/2</sub> ladder of the ground electronic state. Hence, this vibronic mode of the  $\nu_{11}$  vibrational state could be detected in sensitive line surveys of cold sources.

TMC-1 is a cold starless core located in Taurus at a distance of 140 pc (Cernicharo & Guélin 1987). Its kinetic temperature is 10 K and, so far, all observed lines correspond to rotational transitions of a large variety of molecular species in their ground vibrational state. Using the sensitive QUIJOTE<sup>1</sup> line survey (Cernicharo et al. 2021a), we report the detection in TMC-1 of 12 lines of the  $\nu_{11}(\mu^2\Sigma)$  vibrational mode of C<sub>6</sub>H, and of 28 lines of the <sup>2</sup>Π<sub>3/2</sub> and <sup>2</sup>Π<sub>1/2</sub> ladders of its ground electronic state. It is

<sup>★</sup> Based on observations carried out with the Yebes 40m telescope (projects 19A003, 20A014, 20D023, 21A011, 21D005, and 23A024). The 40m radio telescope at Yebes Observatory is operated by the Spanish Geographic Institute (IGN, Ministerio de Transportes, Movilidad y Agenda Urbana).

<sup>1</sup> Q-band Ultrasensitive Inspection Journey to the Obscure TMC-1 Environment

the first time that emission from a vibrationally excited state has been detected in a cold astrophysical environment.

## 2. Observations

The observational data used in this work are part of QUIJOTE (Cernicharo et al. 2021a), a spectral line survey of TMC-1 in the Q-band carried out with the Yebes 40m telescope at the position  $\alpha_{J2000} = 4^{\text{h}}41^{\text{m}}41.9^{\text{s}}$  and  $\delta_{J2000} = +25^{\circ}41'27.0''$ , corresponding to the cyanopolyne peak (CP) in TMC-1. The receiver was built within the Nanocosmos project<sup>2</sup> and consists of two cold high-electron mobility transistor amplifiers covering the 31.0–50.3 GHz band with horizontal and vertical polarisations. Receiver temperatures achieved in the 2019 and 2020 runs vary from 22 K at 32 GHz to 42 K at 50 GHz. Some power adaptation in the down-conversion chains have reduced the receiver temperatures over the course of 2021 to 16 K at 32 GHz and 30 K at 50 GHz. The backends are  $2 \times 8 \times 2.5$  GHz fast Fourier transform (FFT) spectrometers with a spectral resolution of 38 kHz, providing the whole coverage of the Q-band in both polarisations. A more detailed description of the system is given by Tercero et al. (2021).

The data of the QUIJOTE line survey presented here were gathered in several observing runs between November 2019 and July 2023. All observations were performed using frequency-switching observing mode with a frequency throw of 8 and 10 MHz. The total observing time on the source for data taken with frequency throws of 8 MHz and 10 MHz is 465 and 737 hours, respectively. Hence, the total observing time on source is 1202 hours. The measured sensitivity varies between 0.08 mK at 32 GHz and 0.2 mK at 49.5 GHz. The sensitivity of QUIJOTE is around 50 times better than that of previous line surveys in the Q band of TMC-1 (Kaifu et al. 2004). For each frequency throw, different local oscillator frequencies were used in order to remove possible side band effects in the down conversion chain. A detailed description of the QUIJOTE line survey is provided in Cernicharo et al. (2021a). The data analysis procedure has been described in Cernicharo et al. (2022). The main beam efficiency measured during our observations in 2022 varies from 0.66 at 32.4 GHz to 0.50 at 48.4 GHz (Tercero et al. 2021) and can be given across the Q-Band by  $B_{\text{eff}} = 0.797 \exp[-(\nu(\text{GHz})/71.1)^2]$ . The forward telescope efficiency is 0.97. The telescope beam size at half power intensity is  $54.4''$  at 32.4 GHz and  $36.4''$  at 48.4 GHz.

The intensity scale utilised in this study is the antenna temperature ( $T_A^*$ ). Calibration was performed using two absorbers at different temperatures and the atmospheric transmission model ATM (Cernicharo 1985; Pardo et al. 2001). The absolute calibration uncertainty is 10%. However, the relative calibration between lines within the QUIJOTE survey is probably better because all the spectral features have common pointing and calibration errors. The data were analysed with the GILDAS package<sup>3</sup>.

## 3. Results

The line identification in this work was performed using the MADEx code (Cernicharo 2012) and the CDMS catalogue (Müller et al. 2005). The spectroscopy of  $\text{C}_6\text{H}$  in the ground electronic state is directly adopted from the CDMS catalogue.  $\text{C}_6\text{H}$  has been previously observed in its ground electronic state

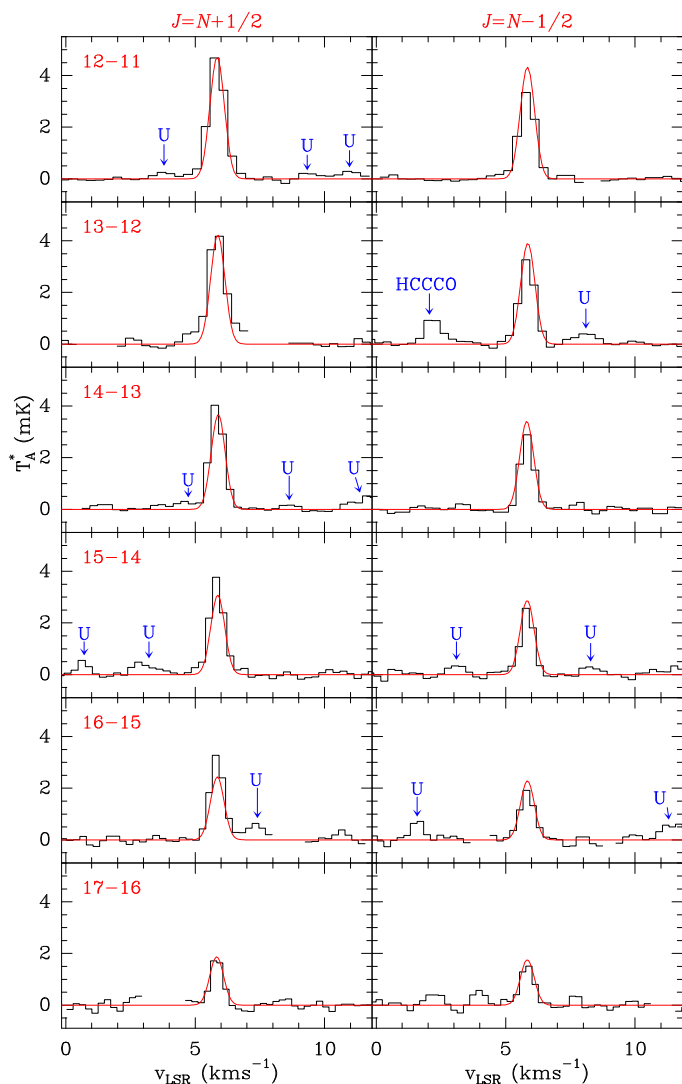


**Fig. 1.** Selected transitions for the excited state of  $\text{C}_6\text{H}$  in TMC-1. Left and right panels correspond to the  $J = N + 1/2$  and  $J = N - 1/2$  components of each transition, respectively. The abscissa corresponds to the local standard of rest (LSR) velocity. The derived line parameters are given in Table B.1. The ordinate is the antenna temperature, corrected for atmospheric and telescope losses, in mK. Blanked channels correspond to negative features produced when folding the frequency-switched data. The quantum numbers of each transition are indicated in the corresponding panel. The red line shows the computed synthetic spectra for this species for  $T_{\text{rot}} = 6.2$  K and a column density of  $1.2 \times 10^{11} \text{ cm}^{-2}$ .

in TMC-1 (Suzuki et al. 1986; Cernicharo et al. 1987). The  $\nu_{11}(\mu^2\Sigma)$  state is highly perturbed and high distortion constants are needed to reproduce the laboratory frequencies (Gottlieb et al. 2010). We fit all laboratory frequencies with distortion constants  $D, H, L$ , and  $M$  for the rotation, as well as  $D$  and  $H$  for the fine structure. The results have been implemented into the MADEx code to predict the frequencies of its rotational and fine structure transitions (see Appendix A). The adopted dipole moment of the molecule is 5.54 D (Woon 1995). We have assumed that it is the same for the  $\nu_{11}(\mu^2\Sigma)$  vibrationally excited state. However, the dipole moment for the rovibrational transitions  $\nu_{11}(\mu^2\Sigma) \rightarrow X^2\Pi$  is unknown. Moreover, the corresponding frequencies would lie in the millimeter and submillimeter frequency domains.

<sup>2</sup> <https://nanocosmos.iff.csic.es/>

<sup>3</sup> <http://www.iram.fr/IRAMFR/GILDAS>

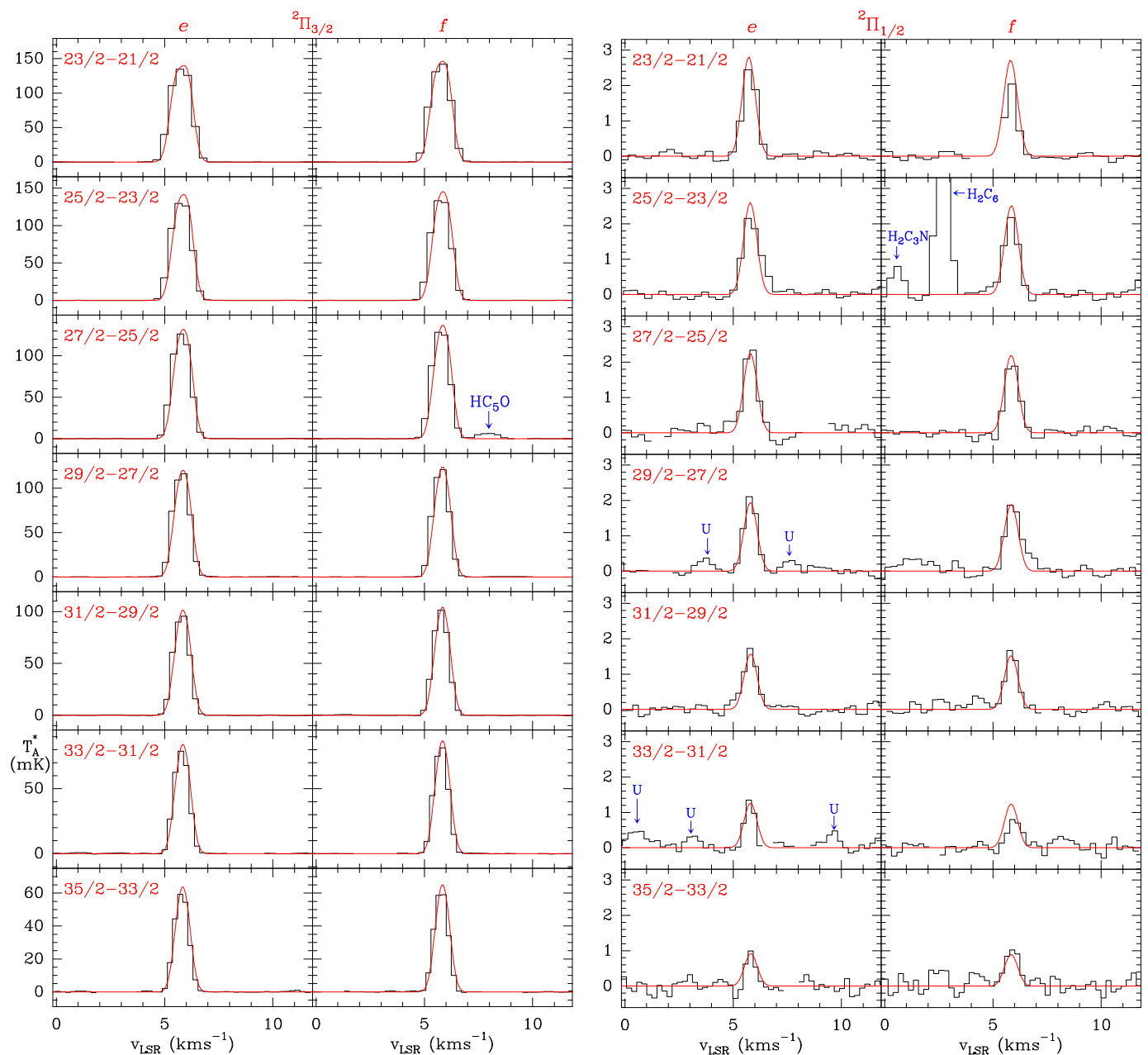


**Fig. 2.** Observed transitions in TMC-1 of the  $^2\Pi_{3/2}$  (two left columns) and  $^2\Pi_{1/2}$  (two right columns) states of C<sub>6</sub>H. The labels *e* and *f* correspond to the Lambda-type doubling components of each transition. The abscissa corresponds to the LSR velocity. The derived line parameters are given in Table B.1. The ordinate is the antenna temperature, corrected for atmospheric and telescope losses, in mK. Blanked channels correspond to negative features produced when folding the frequency-switched data. The quantum numbers of each transition are indicated in the corresponding panel. The red line shows the computed synthetic spectra for this species (see Sect. 3).

We detected a total of 40 lines of C<sub>6</sub>H within the QUIJOTE line survey. Their intensities range from 148 mK to  $\sim$ 1 mK. The derived line parameters are given in Table B.1. Among these lines, we detected 12 transitions of the  $\nu_{11}(\mu^2\Sigma)$  vibrationally excited state. They involve quantum numbers from  $N=12-11$  to  $N=17-16$ . For each rotational transition, two fine structure components were detected ( $J = N + 1/2$  and  $J = N - 1/2$ ; denoted as *a* and *b* in Tables B.1 and B.2). The lines are shown in Fig. 1. The hyperfine splitting of the lines of  $\nu_{11}(\mu^2\Sigma)$  state is smaller than that of the lines in the ground state and does not affect the line widths. Fourteen of the detected lines correspond to the  $^2\Pi_{3/2}$  ladder of the ground electronic state. They are the strongest transitions of C<sub>6</sub>H and their quantum numbers range from  $J =$

$23/2-21/2$  to  $J = 35/2-33/2$ . For the  $^2\Pi_{1/2}$  ladder, we also detected 14 lines involving the same quantum numbers. They are the weakest lines of C<sub>6</sub>H, that is, even weaker than those of the  $\nu_{11}(\mu^2\Sigma)$  state. The two ladders of the ground electronic state show two Lambda-type doubling components for each rotational transition (denoted as *e* and *f* in Table B.1 and in Fig. 2). The observed lines of the ground state are shown in Fig. 2. These lines are slightly broadened due to the hyperfine structure of each line ( $\sim$ 60 and 40 kHz for the  $^2\Pi_{3/2}$  and  $^2\Pi_{1/2}$  ladders, respectively). All the observed frequencies of the ground state are within 5 kHz of the predicted center frequencies for each transition. For the  $\nu_{11}(\mu^2\Sigma)$  mode we have merged the observed frequencies with the laboratory data of Gottlieb et al. (2010) to

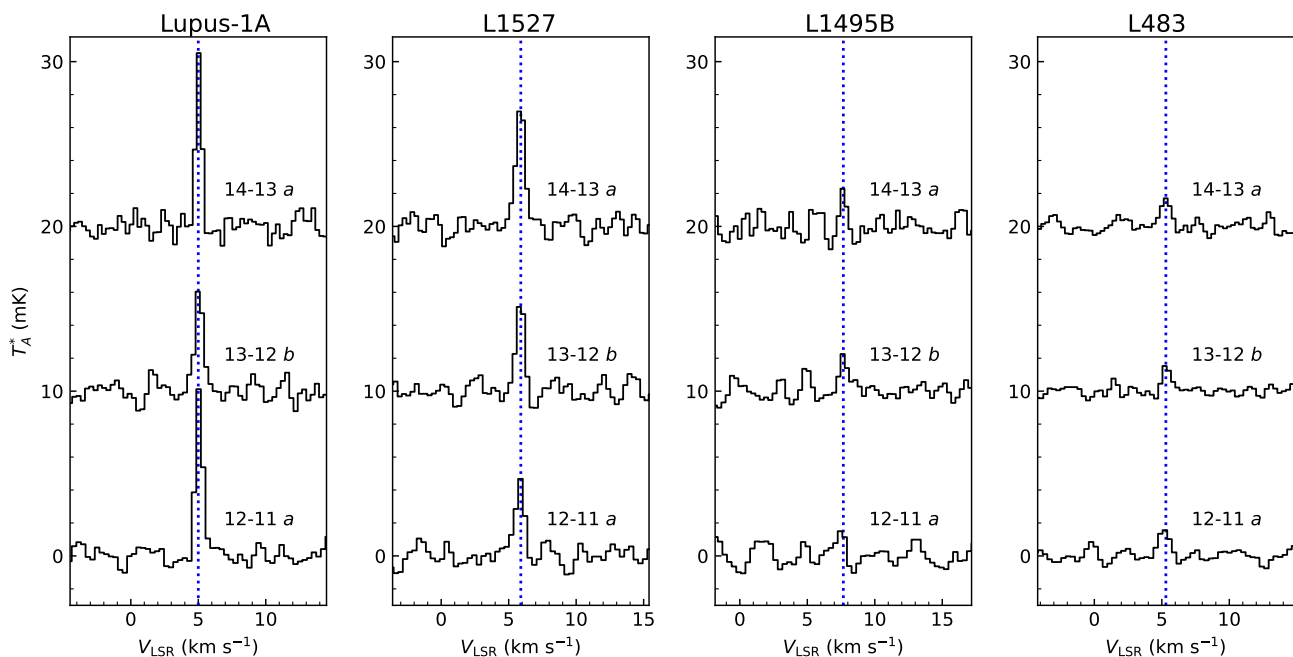


**Fig. 3.** Selected transitions of  $C_6H$   $\nu_{11}(\mu^2\Sigma)$  observed in Lupus-1A, L1527, L1495B, and L483 with the Yebes 40m telescope. Abscissa is the LSR velocity in  $\text{km s}^{-1}$ . The ordinate is the antenna temperature corrected for telescope and atmospheric losses. Line parameters for all observed lines are given in Table B.2.

get an improved set of rotational, fine structure, and distortion constants (see Appendix A).

To estimate the column densities and rotational temperatures, we assumed that the source has a diameter of  $80''$  and that it has an uniform brightness distribution for all observed lines (Fossé et al. 2001, Fuentetaja et al. 2023, in prep.). The adopted intrinsic linewidth is  $0.6 \text{ km s}^{-1}$ . The  $\nu_{11}(\mu^2\Sigma)$  mode is radiatively connected to the  ${}^2\Pi_{3/2}$  and  ${}^2\Pi_{1/2}$  ladders of the ground state. All the levels should be treated simultaneously to solve the statistical equilibrium equations.

Although collisional rates are available for  $C_6H$  in its ground electronic state (Walker et al. 2018), no such rates are available for the  $\nu_{11}(\mu^2\Sigma)$  mode. The energy of the levels involved in the transitions observed for this state, without adding the energy difference between it and the ground state, varies between 10.4 ( $N_u=12$ ) and 20.5 K ( $N_u=17$ ). Consequently,  $T_{rot}$  should be well constrained by the data. To obtain the column density and rotational temperature, we used a model line fitting procedure, adopting a LTE approach (all transitions with identical rotational temperature) in which both parameters are optimised (see e.g. Cernicharo et al. 2021b). We obtain  $T_{rot}=6.2\pm 0.4 \text{ K}$  and  $N(\nu_{11}(\mu^2\Sigma))=(1.2\pm 0.2)\times 10^{11} \text{ cm}^{-2}$ . Using a standard rotational diagram, we obtained similar results. The column density for the  $\nu_{11}(\mu^2\Sigma)$  state is similar to that of  $C_6H^-$  (McCarthy et al. 2006) and to that of many other molecules of the  $C_nH_m$ ,  $C_nH$ ,  $C_nH^-$ , and  $C_nH^+$  families previously analysed with QUIJOTE (Table A.1 of Cernicharo et al. 2022).

For the ground electronic state, we tried to use the collisional rates of  $C_6H$ , with He calculated by Walker et al. (2018) and including the two ladders. However, no satisfactory solutions have been found (see discussion on this point in Agúndez et al. 2023). To roughly reproduce the intensities of the  ${}^2\Pi_{3/2}$  ladder, we have to use a value for  $n(H_2)$  that is uncommon for TMC-1,  $\sim 10^6 \text{ cm}^{-3}$ , without having still a reasonable fit to the lines of the  ${}^2\Pi_{1/2}$  ladder. Rotational temperatures for these high densities are around 6 K and the column density needed to reproduce

the  ${}^2\Pi_{3/2}$  ladder is  $\sim 5\times 10^{12} \text{ cm}^{-2}$ . However, the predicted lines of the  ${}^2\Pi_{1/2}$  ladder are a factor of two stronger than what is observed. Using the line fitting procedure, with the assumption of a common rotational temperature for all levels, we found the same problem if both ladders are treated simultaneously. In both cases, LVG or LTE, the column density that fits the  ${}^2\Pi_{3/2}$  ladder has to be divided by a factor of two to reproduce the intensities of the  ${}^2\Pi_{1/2}$  one. This indicates that the rotational and interladder temperatures are different, and/or that the  ${}^2\Pi_{1/2}$  ladder is sharing a fraction of its population with the  $\nu_{11}(\mu^2\Sigma)$  vibrational mode.

To obtain reasonable values for the column densities in the two ladders of the ground vibrational state, we considered each ladder separately. We derived  $T_{rot}({}^2\Pi_{3/2})=6.2\pm 0.2 \text{ K}$ ,  $T_{rot}({}^2\Pi_{1/2})=6.2\pm 0.4 \text{ K}$ ,  $N({}^2\Pi_{3/2})=(6.2\pm 0.2)\times 10^{12} \text{ cm}^{-2}$ , and  $N({}^2\Pi_{1/2})=(8.0\pm 0.3)\times 10^{10} \text{ cm}^{-2}$ . The calculated synthetic spectra are shown in Fig. 2 and they fit the observed lines of the two ladders remarkably well. From the derived column densities and the energy difference of 22 K between the ladders, it is possible to derive an interladder temperature of  $5.1\pm 0.3 \text{ K}$  (which neglects the contribution of the  $\nu_{11}(\mu^2\Sigma)$  mode). The total column density of  $C_6H$  has to take into account the contribution of the two ladders and of the  $\nu_{11}(\mu^2\Sigma)$  vibrational state. Hence,  $N(C_6H)=(6.4\pm 0.2)\times 10^{12} \text{ cm}^{-2}$ . This value of  $N(C_6H)$  is consistent (within 10%) with that derived previously (see Table A.1 of Cernicharo et al. 2022). The fraction of  $C_6H$  molecules in the  ${}^2\Pi_{3/2}$ ,  ${}^2\Pi_{1/2}$ , and  $\nu_{11}$  states is 96.8%, 1.3%, and 1.9%, respectively. Adopting the energy of 15.8 K for the  $\nu_{11}(\mu^2\Sigma)$  level (Zhao et al. 2011), then the interladder temperature between the ground  ${}^2\Pi_{3/2}$  state and this vibrational level is  $4.0\pm 0.3 \text{ K}$ .

Our failure to reproduce the intensity of the lines when considering the two ladders simultaneously is due to the fact that the rotational levels of the  $\nu_{11}(\mu^2\Sigma)$  state have to be merged with those of  ${}^2\Pi$  ground state. The partition function of  $C_6H$  has to take into account all levels. Taking into account that this vibrational mode is slightly below in energy than the  ${}^2\Pi_{1/2}$  ladder (15.8 versus 22 K), a significant fraction of the level population

in this ladder is transferred to the vibrational mode. Consequently, for future analyses of C<sub>6</sub>H, it will be necessary to consider that the molecule has three ladders: the two spin components of the ground and the low-lying vibrational mode  $\nu_{11}(\mu^2\Sigma)$ .

### 3.1. Detections in other sources

We also detected C<sub>6</sub>H in the  $\nu_{11}(\mu^2\Sigma)$  vibrational state in four additional cold dense clouds, namely Lupus-1A, L1527, L1495B, and L483. These sources were observed with the Yebes40m telescope in the Q band, selected because they exhibit strong emission in the lines of cyanopolynes and radicals, and they serve as a comparative benchmark with TMC-1. Details of these observations can be found in Agúndez et al. (2023). The coordinates of these sources are given in Table B.2. A selection of the detected lines of C<sub>6</sub>H  $\nu_{11}(\mu^2\Sigma)$  is shown in Fig. 3, while the line parameters for all observed transitions are listed in Table B.2. We derived the column densities of C<sub>6</sub>H in the  $\nu_{11}(\mu^2\Sigma)$  state towards Lupus-1A and L1527 through rotational diagrams, assuming that the source fills the beam of the telescope. In the case of Lupus-1A and L1527, there are enough lines to derive a rotational temperature, while for L1495B and L483, there is only a low number of lines; therefore, we fixed the rotational temperature to the values determined for C<sub>6</sub>H in the ground vibrational state (Agúndez et al. 2023). In Lupus-1A, we derived  $T_{rot} = 10.5 \pm 2.1$  K and  $N(\text{C}_6\text{H}, \nu_{11}(\mu^2\Sigma)) = (1.4 \pm 0.5) \times 10^{11}$  cm<sup>-2</sup>; while in L1527, we obtained  $T_{rot} = 30.8 \pm 17.1$  K and  $N(\text{C}_6\text{H}, \nu_{11}(\mu^2\Sigma)) = (1.3 \pm 0.4) \times 10^{11}$  cm<sup>-2</sup>. For Lupus-1A, the rotational temperature derived is consistent with the value of  $10.7 \pm 0.7$  K derived for C<sub>6</sub>H by Agúndez et al. (2023); while in the case of L1527, the rotational temperature is somewhat higher, although it is consistent within the uncertainty, with the value of  $19.6 \pm 3.4$  K derived for C<sub>6</sub>H by Agúndez et al. (2023). For L1495B and L483, we adopted rotational temperatures of 7.0 K and 8.3 K, respectively, and we derived column densities for C<sub>6</sub>H  $\nu_{11}(\mu^2\Sigma)$  of  $6.1 \times 10^{10}$  cm<sup>-2</sup> and  $4.5 \times 10^{10}$  cm<sup>-2</sup>, respectively.

The column density ratios between the  $\nu_{11}(\mu^2\Sigma)$  state and the ground vibrational state of C<sub>6</sub>H are 3.8%, 14.8%, 4.1%, and 6.0% for Lupus-1A, L1527, L1495B, and L483, respectively. These population fractions correspond to interladder temperatures of 4.8, 8.3, 5.0, and 5.6 K, respectively. The vibronic state  $\nu_{11}(\mu^2\Sigma)$  is therefore more populated in these four clouds than in TMC-1, especially in the case of L1527. This latter cloud is known to be significantly warmer than the others (Sakai et al. 2008; Agúndez et al. 2023). It thus seems that the fraction of C<sub>6</sub>H in the vibronic state is correlated with the gas kinetic temperature and the volume density, which suggests that the rotational levels within this vibrationally excited state are mainly populated through collisions. That is to say, the warmer and denser the source, the larger the fractional population of the vibrationally excited state. However, the exact way in which these levels are excited is likely the result of a complex interplay of collisional and radiative processes involving the  $^2\Pi_{3/2}$ ,  $^2\Pi_{1/2}$ , and  $\nu_{11}(\mu^2\Sigma)$  ladders.

## 4. Discussion and conclusions

We report the first detection of an excited vibrational state in cold starless cores. This opens up the possibility that other low-lying vibrationally excited states of abundant species are detected in these types of sources. We also searched for the lines of the  $^2\Delta$  vibronic state, observed towards IRC+10216 (Cernicharo et al. 2008). However, as expected from its energy of  $\sim 60$  K (Zhao et

al. 2011), these lines have not been detected in TMC-1 or in any of the other sources. IRC+10216 represents a warmer environment and infrared radiative pumping plays an important role in the population of the vibrational states of abundant molecules (Cernicharo et al. 2008, 2013, 2014; Pardo et al. 2018). Thermal emission from vibrationally excited states of HC<sub>3</sub>N is often found in warm and hot molecular clouds (de Vicente et al. 2000; Peng et al. 2017; Taniguchi et al. 2022). However, its lowest bending mode is at  $\sim 222$  cm<sup>-1</sup> (Bizzocchi et al. 2017). Hence, we do not expect emission from this vibrational level in cold sources.

The detection of lines from the  $\nu_{11}(\mu^2\Sigma)$  vibrational mode of C<sub>6</sub>H in cold dark clouds indicates that the low energy vibrational levels of abundant molecules have to be considered in the analysis of sensitive line surveys. Lines arising from low-lying vibrationally excited bending states of C<sub>*n*</sub>H and C<sub>*n*</sub>N radicals are potential candidates. Some of these species have a low-lying electronic state close to their ground state that could induce important effects in the energy of their bending vibrational modes (see, e.g. Botschwina et al. 1997). Other molecules have such Renner-Teller interactions lowering the energies of their bending modes. Among the ones that have been fully characterised in the laboratory, we have the  $\nu_4$  mode of C<sub>3</sub>H (Yamamoto et al. 1990) and the  $\nu_7$  mode of C<sub>4</sub>H (Yamamoto et al. 1987; Guélin et al. 1987b; Cooksy et al. 2015). The latter has been observed in IRC+10216 (Guélin et al. 1987b; Cernicharo et al. 2000). However, the rotational transitions arising from these vibrational modes involve energy levels above 30 K and, thus, they were not detected in the sources observed in this work.

We have found that the available collisional rates for C<sub>6</sub>H (Walker et al. 2018) require very high volume densities ( $n(\text{H}_2) \geq 10^6$  cm<sup>-3</sup>) to reproduce the observed intensities and the rotational temperatures derived in our analysis. Refined quantum chemical calculations of these rates are needed, including the  $\nu_{11}$  state, in order to obtain reasonable values for the volume density from the observation of the C<sub>6</sub>H radical in interstellar clouds.

*Acknowledgements.* We thank Ministerio de Ciencia e Innovación of Spain (MICIU) for funding support through projects PID2019-106110GB-I00, PID2019-107115GB-C21 / AEI / 10.13039/501100011033, and PID2019-106235GB-I00. We also thank ERC for funding through grant ERC-2013-Syg-610256-NANOCOSMOS. We would like to thank our referee, Prof. S. Yamamoto, for usefull comments and suggestions.

## References

- Agúndez, M., Marcelino, N., Tercero, B., et al. 2023, *A&A*, 677, A106  
 Bizzocchi, L., Tamassia, F., Lass, J., et al. 2017, *ApJ*, 233, 11  
 Botschwina, P., Horn, M., Markey, K. & Oswald, R. 1997, *Mol. Phys.*, 92, 381  
 Brown, S.T., Rienstra-Kiracofe, R. & Schaefer, H.F. III 1999, *J. Phys. Chem. A*, 103, 4065  
 Cao, Z. & Peyrimhoff, S.D. 2001, *Phys. Chem. Chem. Phys.*, 3, 1403  
 Cernicharo, J. 1985, Internal IRAM report (Granada: IRAM)  
 Cernicharo, J., Guélin, M., Menten, K. & Walmsley, C.M. 1987, *A&A*, 181, L1  
 Cernicharo, J. & Guélin, M. 1987, *A&A*, 176, 299  
 Cernicharo, J., Guélin, M. & Kahane, C. 2000, *A&A S.S.*, 142, 181  
 Cernicharo, J., Guélin, M., Agúndez, M., et al. 2008, *ApJ*, 688, L83  
 Cernicharo, J., 2012, in *ECLA 2011: Proc. of the European Conference on Laboratory Astrophysics*, EAS Publications Series, 2012, Ed.: C. Stehl, C. Joblin, & L. d'Hendecourt (Cambridge: Cambridge Univ. Press), 251; [https://nanocosmos.iff.csic.es/?page\\_id=1619](https://nanocosmos.iff.csic.es/?page_id=1619)  
 Cernicharo, J., Daniel, F., Castro-Carrizo, A. et al. 2013, *ApJ*, 778, L25  
 Cernicharo, J., Teyssier, D., Quintana-Lacaci, G. et al. 2014, *ApJ*, 796, L21  
 Cernicharo, J., Agúndez, M., Kaiser, R., et al. 2021a, *A&A*, 652, L9  
 Cernicharo, J., Cabezas, C., Endo, Y., et al. 2021b, *A&A*, 646, L3  
 Cernicharo, J., Fuentetaja, R., Agúndez, M. et al. 2022, *A&A*, 663, L9  
 Cooksy, A. L., Gottlieb, C. A., Killian, T. C. et al. 2015, *ApJS*, 216, 30  
 de Vicente, P., Martín-Pintado, J. & Colom, P. 2000, *A&A*, 361, 1058  
 Fossé, D., Cernicharo, J., Gerin, M., Cox, P. 2001, *ApJ*, 552, 168

- Fuentetaja, R. et al. 2023, in preparation
- Gottlieb, C. A., McCarthy, M. C., & Thaddeus, P. 2010, *ApJS*, 189, 261.
- Guélin, M., Cernicharo, J., Kahane, C. et al. 1987, *A&A*, 175, L5
- Guélin, M., Cernicharo, J., Navarro, S. et al. 1987b, *A&A*, 182, L37
- Kaifu, N., Ohishi, M., Kawaguchi, K., et al. 2004, *PASJ*, 56, 69
- Linnartz, H., Motylewski, T., Vaizert, O., et al. 1999, *Journal of Molecular Spectroscopy*, 197, 1
- McCarthy, M. C., Gottlieb, C. A., Gupta, H., et al. 2006, *ApJ*, 652, L141
- Müller, H. S. P., Schlöder, F., Stutzki, J., Winnewisser, G. 2005, *J. Mol. Struct.*, 742, 215
- Murakami, A., Kawaguchi, K. & Saito, S. 1988, *Pub. Astron. Soc. Japan*, 39, 189
- Pardo, J. R., Cernicharo, J., Serabyn, E. 2001, *IEEE Trans. Antennas and Propagation*, 49, 12
- Pardo, J. R., Cernicharo, J., Velilla-Prieto, L. et al. 2018, *A&A*, 615, L4
- Pearson, J. C., Gottlieb, C. A., Woodward, D. R. & Thaddeus, P. 1988, *A&A*, 189, L3
- Peng, Y., Qin, S.L., Schilke, P. et al. 2017, *ApJ*, 837, 49
- Sakai, N., Sakai, T., Hirota, T. & Yamamoto, S. 2008, *ApJ*, 672, 371
- Suzuki, H., Ohishi, M., Kaifu, N., et al. 1986, *PASJ*, 38, 911
- Taniguchi, K., Tanak, K.E.I., Zhang, Y. et al. 2022, *ApJ*, 931, 99
- Tercero, F., López-Pérez, J. A., Gallego, et al. 2021, *A&A*, 645, A37
- Walker, K. M., Lique, F., & Dawes, R. 2018, *MNRAS*, 473, 1407
- Woon, D. E. 1995, *Chemical Physics Letters*, 244, 45.
- Yamamoto, S. Shuji, S., Guélin, M. et al. 1987, *ApJ*, 323, L149
- Yamamoto, S. Shuji, S., Suzuki, H. et al. 1990, *ApJ*, 348, 363
- Zhao, D., Haddad, M. A., Linnartz, H., et al. 2011, *J. Chem. Phys.*, 135, 044307.

**Table A.1.** Rotational and distortion constants C<sub>6</sub>H  $\nu_{11}({}^2\Sigma)$ .

Constant <sup>a</sup> (MHz)	Laboratory <sup>b</sup>	Laboratory <sup>c</sup>	Laboratory+TMC-1 <sup>d</sup>
$B$	1394.64000(4)	1394.63997(6)	1394.64004(5)
$10^6 D$	46.48(3)	46.208(63)	46.243(58)
$10^{12} H$	27(7)	-116(26)	-108(25)
$10^{16} L$	-37(5)	220(44)	211(43)
$10^{18} M$		-1.51(25)	-1.47(25)
$\gamma$	-18.826(2)	-18.85682(26)	-18.85434(22)
$10^3 \gamma_D$	2.927(3)	2.9346(31)	2.9350(30)
$10^6 \gamma_H$	-0.1164(9)	-0.11745(93)	-0.11764(89)
$10^{12} \gamma_L$	3.67(7)	3.730(72)	3.747(69)
$N_{lines}$	59	59	71
$\sigma$ (kHz)		15.6	14.1

**Notes.**

<sup>(a)</sup> All constants in MHz. The uncertainties (in parentheses) are in units of the last significant digits.

<sup>(b)</sup> Rotational and distortion constants given by Gottlieb et al. (2010).

<sup>(c)</sup> Rotational and distortion constants derived from a fit to the laboratory data including the distortion constant  $M$ . The hyperfine constants  $b_F$  and  $c$  have been fixed to the values given by Gottlieb et al. (2010).

<sup>(d)</sup> Rotational and distortion constants derived from a fit to the laboratory and TMC-1 data. The hyperfine constants  $b_F$  and  $c$  have been fixed to the values given by Gottlieb et al. (2010). The distortion constant  $M$  has been included to improve the quality of fit.

**Appendix A: Improved rotational constants for C<sub>6</sub>H  $\nu_{11}({}^2\Sigma)$** 

The  $\nu_{11}(\mu^2\Sigma)$  state is highly perturbed and high distortion constants ( $D, H, L$ ) are needed to reproduce the laboratory frequencies (Gottlieb et al. 2010). Although the predicted frequencies for the lines of this state within the QUIJOTE line survey fit the observed ones reasonably well, we have included them in a merged fit to all laboratory and space lines. The distortion constants  $D, H, L$ , and  $M$  for the rotation, and  $D$  and  $H$  for the fine structure have been included. The results are given in Table A.1 and correspond to the recommended constants to predict the frequencies of the  $\nu_{11}({}^2\Sigma)$  state. The table also gives the constants derived by Gottlieb et al. (2010) and those derived from the same set of measurements but including the distortion constant,  $M$ .

**Appendix B: Line parameters**

Line parameters for all observed transitions were derived by fitting a Gaussian line profile to them using the GILDAS package. A velocity range of  $\pm 20 \text{ km s}^{-1}$  around each feature was considered for the fit after a polynomial baseline was removed. Negative features produced in the folding of the frequency switching data were blanked before baseline removal. The derived line parameters for TMC-1 are given in Table B.1 and in Table B.2 for the other sources.

**Table B.1.** Observed line parameters for C<sub>6</sub>H in the  $\nu_{11}(\mu^2\Sigma)$  excited and ground states in TMC-1.

State	Transition <sup>(S)</sup>		$\nu_{rest}^a$ (MHz)	$\int T_A^* dv^b$ (mK km s <sup>-1</sup> )	$v_{LSR}$ (km s <sup>-1</sup> )	$\Delta v^c$ (km s <sup>-1</sup> )	$T_A^{*d}$ (mK)		
$\nu_{11}({}^2\Sigma)$	12-11	<i>a</i>	33462.231±0.010	3.92±0.11	5.83	0.77±0.03	4.78±0.07	A	
	12-11	<i>b</i>	33479.823±0.010	2.77±0.07	5.83	0.77±0.02	3.40±0.07		
	13-12	<i>a</i>	36251.528±0.010	3.78±0.10	5.83	0.82±0.03	4.20±0.12		
	13-12	<i>b</i>	36268.909±0.010	2.41±0.05	5.83	0.69±0.02	3.27±0.07		
	14-13	<i>a</i>	39040.824±0.010	2.89±0.07	5.83	0.66±0.03	4.11±0.08		
	14-13	<i>b</i>	39057.965±0.010	1.95±0.06	5.83	0.63±0.02	2.92±0.09		
	15-14	<i>a</i>	41830.108±0.010	2.65±0.10	5.83	0.67±0.03	3.71±0.11		
	15-14	<i>b</i>	41847.005±0.010	1.66±0.09	5.83	0.60±0.04	2.61±0.12		
	16-15	<i>a</i>	44619.383±0.010	2.30±0.10	5.83	0.66±0.03	3.27±0.12		
	16-15	<i>b</i>	44636.019±0.010	1.37±0.13	5.83	0.68±0.08	1.88±0.12		
	17-16	<i>a</i>	47408.647±0.010	1.12±0.12	5.83	0.55±0.07	1.92±0.13		
	17-16	<i>b</i>	47425.006±0.010	1.03±0.13	5.83	0.61±0.09	1.58±0.16		
${}^2\Pi_{3/2}$	23/2-21/2	<i>e</i>	31881.860±0.002	173.68±0.06	5.74±0.01	1.12±0.01	146.04±0.08		
		<i>f</i>	31885.541±0.002	175.02±0.13	5.73±0.01	1.09±0.01	150.28±0.09		
	25/2-23/2	<i>e</i>	34654.037±0.002	156.89±0.14	5.74±0.01	1.05±0.01	140.59±0.07		
		<i>f</i>	34658.383±0.002	156.17±0.09	5.74±0.01	1.01±0.01	144.69±0.09		
	27/2-25/2	<i>e</i>	37426.192±0.002	139.15±0.05	5.75±0.01	0.97±0.01	134.46±0.09		
		<i>f</i>	37431.255±0.002	138.02±0.14	5.74±0.01	0.94±0.01	138.84±0.09		
	29/2-27/2	<i>e</i>	40198.323±0.002	118.21±0.12	5.76±0.01	0.90±0.01	123.29±0.09		
		<i>f</i>	40204.157±0.002	118.74±0.12	5.75±0.01	0.88±0.01	127.34±0.09		
	31/2-29/2	<i>e</i>	42970.432±0.002	91.80±0.10	5.76±0.01	0.85±0.01	100.94±0.12		
		<i>f</i>	42977.089±0.002	91.76±0.10	5.75±0.01	0.82±0.01	104.66±0.11		
	33/2-31/2	<i>e</i>	45742.519±0.002	70.27±0.12	5.77±0.01	0.80±0.01	82.28±0.14		
		<i>f</i>	45750.052±0.002	70.28±0.13	5.76±0.01	0.77±0.01	85.29±0.16		
35/2-33/2	<i>e</i>	48514.584±0.002	51.51±0.16	5.77±0.01	0.78±0.01	62.27±0.18			
	<i>f</i>	48523.044±0.002	51.00±0.15	5.76±0.01	0.75±0.01	63.69±0.17			
${}^2\Pi_{1/2}$	23/2-21/2	<i>e</i>	32095.245±0.003	2.07±0.09	5.76±0.02	0.75±0.04	2.58±0.08	B	
		<i>f</i>	32125.561±0.003	1.42±0.08	5.83±0.01	0.65±0.04	2.07±0.10		
	25/2-23/2	<i>e</i>	34887.115±0.003	2.25±0.07	5.84±0.02	0.98±0.03	2.17±0.08		
		<i>f</i>	34917.885±0.003	1.86±0.06	5.83±0.01	0.79±0.03	2.21±0.08		
	27/2-25/2	<i>e</i>	37678.938±0.003	1.91±0.13	5.80±0.03	0.72±0.06	2.50±0.17		C
		<i>f</i>	37710.199±0.002	1.62±0.06	5.89±0.02	0.73±0.03	2.11±0.09		
	29/2-27/2	<i>e</i>	40470.713±0.003	1.61±0.08	5.79±0.02	0.70±0.04	2.17±0.08		
		<i>f</i>	40502.502±0.003	1.75±0.13	5.95±0.03	0.88±0.08	1.87±0.12		
	31/2-29/2	<i>e</i>	43262.437±0.003	1.36±0.10	5.79±0.03	0.77±0.07	1.65±0.11		
		<i>f</i>	43294.790±0.003	1.21±0.10	5.85±0.03	0.66±0.07	1.73±0.10		
	33/2-31/2	<i>e</i>	46054.109±0.003	0.80±0.10	5.76±0.03	0.53±0.07	1.42±0.11		
		<i>f</i>	46087.062±0.003	0.64±0.10	6.01±0.05	0.74±0.12	0.82±0.13		
35/2-33/2	<i>e</i>	48845.727±0.003	0.53±0.10	5.81±0.05	0.48±0.09	1.03±0.18			
	<i>f</i>	48879.315±0.003	0.86±0.12	5.89±0.05	0.75±0.12	1.08±0.17			

**Notes.** <sup>(S)</sup> The *a* and *b* labels refers to the  $J = N + 1/2$  and  $J = N - 1/2$  fine components of the  $\nu_{11}({}^2\Sigma)$  state. The *e* and *f* labels correspond to the two lambda-doubling components of the  ${}^2\Pi_{3/2}$  and  ${}^2\Pi_{1/2}$  ladders of the  ${}^2\Pi$  ground electronic state. <sup>(a)</sup> Predicted frequencies for the transitions of C<sub>6</sub>H in MHz. These frequencies are the observed ones for the  $\nu_{11}$  vibrational state assuming a  $v_{LSR}$  of 5.83 km s<sup>-1</sup> (see text). <sup>(b)</sup> Integrated line intensity in mK km s<sup>-1</sup>. <sup>(c)</sup> Line width at half intensity using a Gaussian fit in the line profile (in km s<sup>-1</sup>). For the  ${}^2\Pi_{3/2}$  and  ${}^2\Pi_{1/2}$  ladders of the ground state the lines are slightly broadened by the presence of two hyperfine components, which in addition produce a shift of a few kHz to the center frequency. The broadening decreases when *J* increases. <sup>(d)</sup> Antenna temperature (in mK). <sup>(A)</sup> Only data from the observations with a frequency switching of 8 MHz. <sup>(B)</sup> The line is partially affected by a negative feature. <sup>(C)</sup> Only data from the observations with a frequency switching of 10 MHz.



**Table B.2.** Observed line parameters for C<sub>6</sub>H  $\nu_{11}(\mu^2\Sigma)$  in Lupus-1A, L1527, L1495B, and L483.

Transition	$\nu_{calc}$ (MHz)	$\int T_A^* dv$ (mK km s <sup>-1</sup> )	$\nu_{LSR}$ (km s <sup>-1</sup> )	$\Delta v$ (km s <sup>-1</sup> )	$T_A^*$ (mK)
Lupus-1A ( $\alpha_{2000}=15^h 42^m 52.4^s$ , $\delta_{2000}=-34^{\circ} 07' 53.5''$ )					
12-11 <i>a</i>	33462.222	6.94±0.32	5.07±0.02	0.64±0.03	10.20±0.46
12-11 <i>b</i>	33479.823	5.13±0.34	5.12±0.02	0.67±0.05	7.18±0.48
13-12 <i>a</i>	36251.521	6.09±0.47	5.03±0.02	0.58±0.05	9.95±0.60
13-12 <i>b</i>	36268.907	4.82±0.50	5.05±0.04	0.74±0.10	6.15±0.56
14-13 <i>a</i>	39040.815	5.97±0.39	5.04±0.02	0.53±0.03	10.62±0.68
14-13 <i>b</i>	39057.968	5.34±0.50	5.05±0.03	0.56±0.07	8.89±0.81
15-14 <i>a</i>	41830.101	4.50±0.52	5.05±0.03	0.49±0.07	8.62±0.92
15-14 <i>b</i>	41847.006	2.81±0.46	5.11±0.04	0.37±0.13	7.09±0.89
16-15 <i>a</i>	44619.378	5.37±0.59	5.06±0.03	0.53±0.07	9.49±1.10
16-15 <i>b</i>	44636.019	3.80±0.65	5.16±0.06	0.66±0.14	5.38±1.03
17-16 <i>a</i>	47408.645	3.80±0.82	5.11±0.05	0.50±0.13	7.13±1.85
17-16 <i>b</i>	47425.006	4.07±1.40	5.20±0.10	0.60±0.25	6.32±2.43
L1527 ( $\alpha_{2000}=4^h 39^m 53.9^s$ , $\delta_{2000}=+26^{\circ} 03' 11.0''$ )					
12-11 <i>a</i>	33462.222	3.88±0.41	5.83±0.04	0.79±0.10	4.59±0.52
12-11 <i>b</i>	33479.823	2.74±0.31	5.97±0.04	0.69±0.08	3.72±0.44
13-12 <i>a</i>	36251.521	6.48±0.47	5.88±0.03	0.91±0.08	6.71±0.59
13-12 <i>b</i>	36268.907	4.19±0.37	5.85±0.03	0.69±0.07	5.71±0.54
14-13 <i>a</i>	39040.815	6.26±0.35	5.88±0.02	0.80±0.05	7.33±0.47
14-13 <i>b</i>	39057.968	5.48±0.47	5.84±0.04	1.05±0.11	4.92±0.55
15-14 <i>a</i>	41830.101	4.59±0.53	5.84±0.03	0.52±0.08	8.23±0.92
15-14 <i>b</i>	41847.006	5.09±0.54	5.97±0.03	0.64±0.08	7.51±0.83
16-15 <i>a</i>	44619.378	5.65±0.39	5.79±0.02	0.62±0.05	8.62±0.83
16-15 <i>b</i>	44636.019	4.10±0.58	5.89±0.05	0.74±0.13	5.24±0.84
17-16 <i>a</i>	47408.645	4.85±0.58	5.88±0.04	0.64±0.08	7.15±1.02
17-16 <i>b</i>	47425.006	3.98±0.76	5.90±0.06	0.69±0.17	5.40±1.17
L1495B ( $\alpha_{2000}=4^h 15^m 41.8^s$ , $\delta_{2000}=+28^{\circ} 47' 46.0''$ )					
12-11 <i>a</i>	33462.222	1.20±0.37	7.44±0.13	0.70±0.23	1.60±0.51
12-11 <i>b</i>	33479.823	1.42±0.36	7.87±0.10	0.78±0.22	1.72±0.48
13-12 <i>a</i>	36251.521	2.02±0.38	7.58±0.07	0.78±0.18	2.43±0.41
13-12 <i>b</i>	36268.907	1.64±0.39	7.69±0.08	0.70±0.22	2.19±0.51
14-13 <i>a</i>	39040.815	1.20±0.29	7.67±0.06	0.47±0.11	2.40±0.53
14-13 <i>b</i>	39057.968	1.46±0.42	7.76±0.09	0.57±0.16	2.40±0.73
15-14 <i>a</i>	41830.101	2.13±0.49	7.64±0.04	0.43±0.16	4.68±0.91
L483 ( $\alpha_{2000}=18^h 17^m 29.8^s$ , $\delta_{2000}=-4^{\circ} 39' 38.3''$ )					
12-11 <i>a</i>	33462.222	1.59±0.23	5.16±0.07	0.89±0.13	1.68±0.30
13-12 <i>b</i>	36268.907	1.19±0.18	5.35±0.06	0.70±0.12	1.61±0.24
14-13 <i>a</i>	39040.815	1.53±0.26	5.29±0.07	0.83±0.15	1.73±0.36
15-14 <i>b</i>	41847.006	0.90±0.19	5.26±0.05	0.47±0.09	1.82±0.35
16-15 <i>b</i>	44636.019	1.62±0.34	5.43±0.07	0.63±0.14	2.43±0.58